

25 Modification of Materials by MeV Ion Beams

Y. Zhang¹ and H.J. Whitlow^{2,3}

¹ Pacific Northwest National Laboratory, P O Box 999, Richland, WA 99352, USA
Yanwen.Zhang@pnl.gov

² Department of Physics, P.O. Box 35 (YFL), FIN-40014 University
of Jyväskylä, Finland

Harry_J.Whitlow@phys.jyu.fi

³ School of Technology and Society, Malmö högskola, 206 05 Malmö, Sweden
Harry_J.whitlow@ts.mah.se

25.1 Introduction

Today's fast-developing technologically based society places ever accelerating demands on new materials and materials-processing methods. Leading-edge fields as diverse as biomedical tissue engineering, quantum devices, optical and magnetic information storage technology, and immobilization of actinides all require nanoscale engineering through controlled materials modification. The evolution of these advances from the research science stage to the industrial-applications phase is a particularly challenging task.

Amongst the beam-processing methods (electron, X-ray, laser etc.) for materials modification, MeV ions occupy a unique place. They interact strongly with both the atomic and the electronic structures of the target material to produce a broad plethora of modifications with well-defined penetration characteristics. These modifications can be precisely controlled because MeV ions can be steered and focused using electrostatic and magnetic fields, and also close process control is possible because their delivery can be monitored electrically.

A comprehensive review of materials engineering with MeV ions will not be attempted here. Instead, the scope of this chapter is to introduce the basic concepts with some practical examples of their use in advanced materials engineering.

25.2 Characteristics of MeV Ion Bombardment for Materials Engineering

Ions penetrating matter can modify the material by direct implantation of a foreign atom into the target material, or as a result of the ion stopping, which deposits kinetic energy from the projectile ion into the material. This deposition of energy takes place, as discussed in Chap. 24, by scattering of

the ion by the electrons and nuclei in the target [1]. The coupling of the deposited energy to the electronic and structural system of the material results in a wide plethora of primary effects, illustrated schematically in Fig. 25.1. From the viewpoint of materials modification, we are generally interested in persistent changes such as amorphization of the crystalline structure. These modifications may be *direct*, where no further processing is needed, or *latent*, where an additional stage of processing is required to achieve the desired modification, such as lithography, where the latent image is brought forth by development. The relative importance of the different processes depends on the nature of the material, for example, for dielectric materials the electronic processes are of great importance, whilst for metals, where the electronic excitation relaxes almost instantaneously via electron–phonon interactions, modifications induced by nuclear displacement dominate.

The energy transferred in an individual collision with an MeV ion may be large, extending to keV energies for electrons and MeV for recoiling nuclei. It follows that these recoiling particles can themselves scatter, creating a cascade of energetic secondary electrons and recoil nuclei. As the energies of the primary ion and secondary particles decrease, a very wide plethora of processes take place, as shown in Fig. 25.1. The secondary particles in turn will cause tertiary processes, such as defect agglomeration, forming extended defects such as dislocations and voids; chemical-bond scission; and other forms of

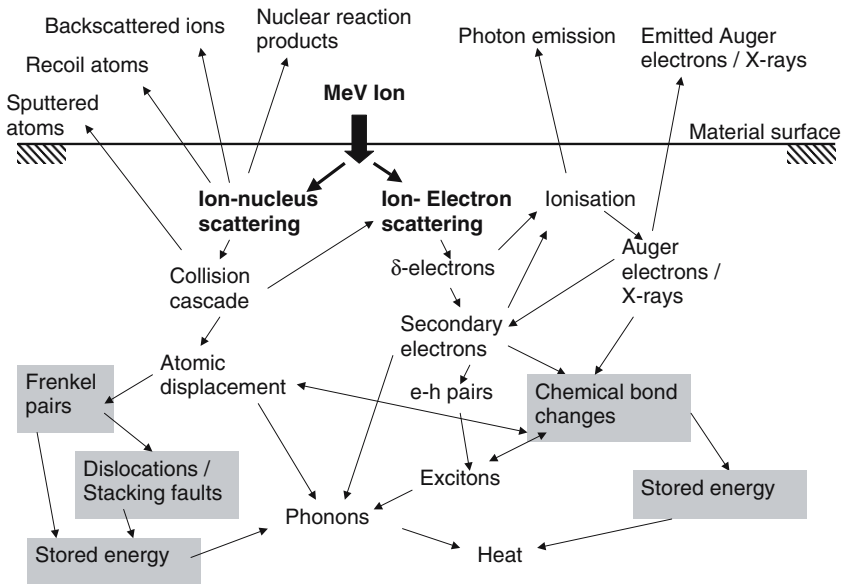


Fig. 25.1. Schematic illustration of the evolution of the processes taking place in a solid material irradiated with MeV ions. The processes shaded gray correspond to long-term effects

radiolysis. In addition, various forms of prompt processes, such as phonon creation, secondary electron emission, sputtering, X-ray and visible photon emission, and backscattering, can take place. Prompt emissions are generally not important for modification, but can be utilized as a monitor signal for process control. It is useful to bear in mind that at any time, the energy balance requires that the energy deposited in the material per ion is the sum of the energy of emitted particles, moving particles, stored energy associated with induced defects, chemical-bond changes and heat. Moreover, the sum of the momentum of all moving particles in the cascade must sum to the primary-ion momentum.

25.2.1 Fundamental Interactions Between MeV Ions and Materials

As an energetic ion penetrates the surface of matter, the probability of scattering with electrons and the atomic nuclei of the material rises from zero outside of the material to some finite value determined by the appropriate cross section (Chap. 24). The successive scattering from atomic nuclei and electrons along the ion trajectory gives rise to a stopping force¹ on the projectile, transferring energy to the target material. This slowing down gives rise to the two basic forms of ion beam modification of materials:

- i. If the material is thick enough, the ion, after traversing a distance R , where

$$R = \int_E^0 \frac{dE}{(-dE/dx)} \quad (25.1)$$

termed the range, will lose all its energy because of the stopping force and come to rest. This process, termed ion implantation, is widely used to modify materials by introducing foreign atoms.

- ii. The material is modified through deposition of energy by interaction with the ion, which induces chemical, structural and electronic changes.

25.2.2 Characteristics of MeV Ion Penetration

The salient features of MeV ion bombardment are illustrated in Fig. 25.2, which presents the results from SRIM binary collision approximation (BCA) model calculations [2] of 7 MeV ^{14}N ions (0.5 MeV per nucleon) incident on a Si target. This combination was chosen because it represents an intermediate-mass target and an intermediate-mass ion with an energy that can easily be obtained from both single-ended and tandem MeV ion accelerators. It is evident from this figure that:

¹ The stopping force ($-dE/dx$) is, strictly incorrectly, often termed the stopping power. See Appendix 25.A.

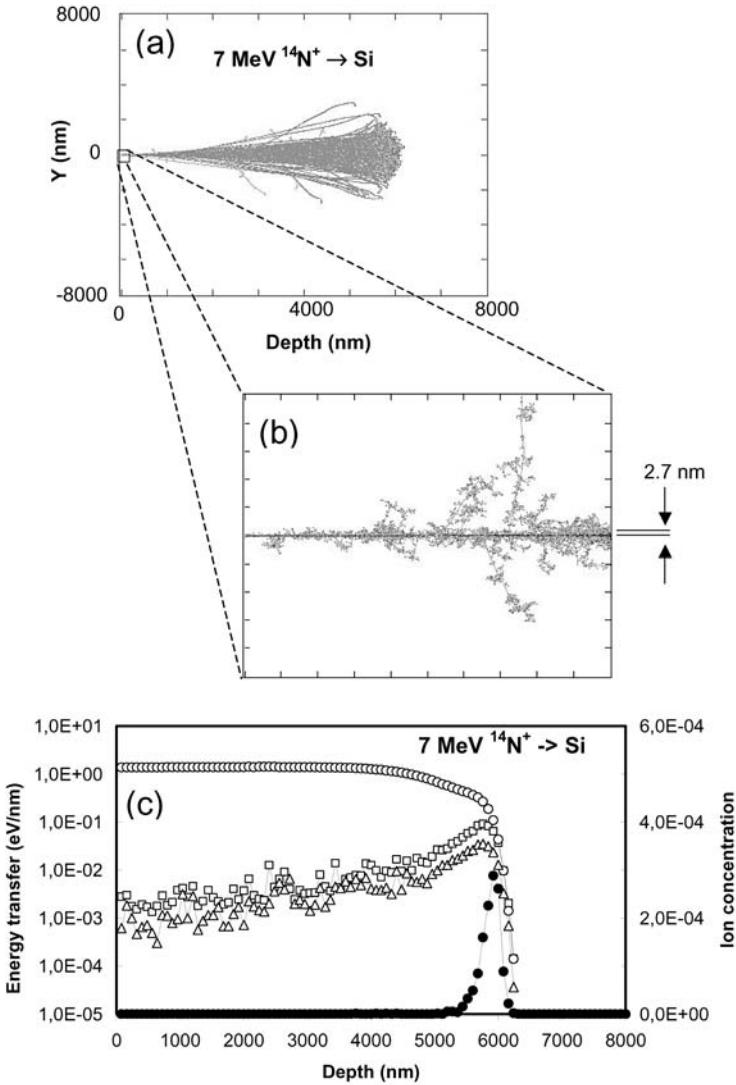


Fig. 25.2. SRIM simulation [2] of 7 MeV ^{14}N ions impinging on an amorphous Si target. The ion–target combination represents an intermediate-mass ion on an intermediate-mass target material. (a) Whole depth region, showing the deep penetration. (b) 100 nm thick, 200 nm wide surface region, showing the small spreading of the primary ions. (c) Depth distribution of ion projected range (*closed circles*), energy deposited as primary ionization (*open circles*), energy deposited in creating nuclear recoils (*open squares*) and energy deposited in ionization by nuclear recoils (*open triangles*)

- i. Almost all of the ions come to rest at a depth of $\sim 5.8 \mu\text{m}$ with a straggling of $\sim 1 \mu\text{m}$. The ratio of the straggling to the projected range is much less than for low-energy (keV) ions.
- ii. Energy deposition in electronic excitations dominates the stopping process.
- iii. Energy deposition in nuclear scattering processes takes place along the entire ion track but is an order of magnitude smaller than the electronic energy deposition. These processes are largest close to the end of the ion range. The majority of the energy deposited in nuclear scattering ends up as electronic excitation through electronic stopping of the energetic recoils.
- iv. At the end of the range, the lateral radial spreading of the trajectories is large ($\sim 400 \text{ nm}$). However, in the near-surface region, where only little nuclear scattering takes place, the radial spreading of the trajectories is correspondingly small ($\sim 3 \text{ nm}$). Although in this near-surface region there is radial transport of energy by nuclear recoils, the overwhelming contribution to the electronic energy deposition comes from the primary ions.

25.2.3 Nuclear Collision Cascades

The dynamics of nuclear collision cascades are described in Chap. 24; therefore, only a cursory treatment will be given here. In contrast to the case for keV ion irradiation, the mean free path for nucleus–nucleus scattering is large. This results in small, isolated subcascades along the primary-ion trajectory. These can be seen extending sideways in Fig. 25.2(b). This is particularly the case close to the surface, where the cross section for nuclear scattering is small and the mean free path between nuclear scattering events is correspondingly large. For nanometer materials, the structures are often just a few hundred nm thick. Thus MeV ions will pass through these structures creating very few cascades compared with the case for keV ions.

Nuclear collisions lead to the formation of Frenkel pairs. A *Frenkel pair* is composed of two point defects: a *vacancy*, which is a site where an atom would normally be located, and an *interstitial*, which is a site where an atom is located that would not normally be there. The situation for MeV ions is very closely similar to that for low-energy ion bombardment. The process is essentially the same for other forms of irradiation, and the physics is discussed in detail in the book by Thompson [3] and the compendium by Andersen [4]. If the interstitial and its associated vacancy are close together, they can undergo correlated recombination, and the defect energies are then converted to phonons (heat). Alternatively, the interstitial may be annihilated at another vacancy (uncorrelated recombination) or a defect sink, again releasing heat. The effect of the buildup of primary defects may lead to their agglomeration to form so-called extended defects such as voids, dislocations stacking and faults [1, 3]. If the fluence is sufficiently large, these amorphous subdomains

overlap and a layer that is totally amorphous will form. The defects produced during the slowing processes are not thermalized. This can be utilized in defect-stimulated regrowth of amorphous layers and domains [1].

25.2.4 Electronic Processes

Electron Cascades

In addition to the nuclear collision cascade processes discussed above (Sect. 25.2.3 and Chap. 24), the electronic stopping of the primary ion and secondary recoil nuclei can induce materials modification. The electronic stopping for MeV ions is much greater than the nuclear stopping, and consequently electron-induced materials modification by MeV ions may be more pronounced than for keV ions, where the contribution from nuclear stopping is more prominent. The electronic stopping creates excited electrons by ion–electron scattering. This scattering can excite electrons in both the projectile and the target atoms [5], from both core and valence electron levels, to unfilled bound states (so-called *resonant excitation*) or to free states (*quasi-classical scattering*) [6]. For quasi-classical scattering, the energy of the scattered free electron is $E_f = T - E_b$, where $T \approx E (4m_e/M_1) \cos^2 \varphi$ is the energy transferred to a free electron in an ion–electron collision with an ion of mass M_1 , where E_b is the electron binding energy. For valence electrons E_b is of the order of a few eV and we may, to a good approximation, consider them to be free classical electrons ($E_b = 0$). The primary electrons (δ -electrons) will then have energies extending from zero ($\varphi = \pi/2$) to a maximum T_{max} at $\varphi = 0$ (see Fig. 25.3), which corresponds to 2.2 keV for 1 MeV protons. The δ -electrons undergo elastic and inelastic scattering with the target electrons as they move through the target material. In the scattering process, the δ -electrons transfer kinetic energy to the target electrons, resulting in a cascade of secondary electrons, shown schematically in Fig. 25.3. The energy deposited in the scattering process can lead to modification of the material, for example by breaking and forming chemical bonds in dielectric materials around the ion track. The extent of the secondary-electron-induced modification will then be governed by the dose at that point in the material. In general, the ion track dose model [7] is a good starting point. The differential cross section $d\sigma$ for an energy transfer T to $T + dT$ between an ion of charge Z_1e and an electron is

$$d\sigma = \frac{Z_1^2 e^4 dT}{8\pi\epsilon_0^2 m_e v_1 T^2} \quad (25.2)$$

Note that this expression (25.2), in SI units, differs from the cgs counterpart usually quoted (with $e^2 \Rightarrow e^2/4\pi\epsilon_0$) and that Z_1 can be an effective charge. The energy transfer T depends on the recoil angle (Fig. 25.3). The number n of δ -electrons scattered through φ to $\varphi + d\varphi$ becomes, by substitution for dT/T^2 and $M_1 = 2E/v_1^2$,

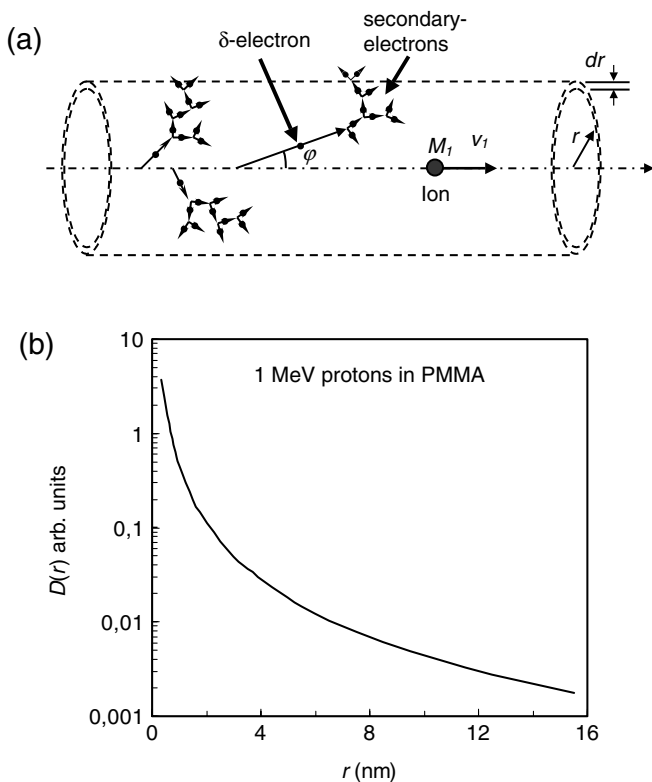


Fig. 25.3. (a) Schematic illustration of secondary-electron cascades for an MeV ion moving through matter. (b) Radial electron energy dose distribution $D(r)$ for 1 MeV protons in poly(methylmethacrylate) (PMMA). Note that the $D(r)$ scale is logarithmic

$$dn = N_e \frac{Z_1^2 e^4 \sin \varphi}{8\pi \epsilon_0^2 m_e v_1 \cos^3 \varphi} d\varphi \quad (25.3)$$

The cross section dn approaches infinity asymptotically for $\varphi \rightarrow \pi/2$, and the majority of δ -electrons are directed perpendicular to the beam, with energies T close to zero. δ -electrons scattered with smaller φ will have greater energy T . The range of electrons in the material can be conveniently approximated by the empirical relation

$$R(T) = (\alpha/\rho)T^\beta \quad (25.4)$$

where $a = 5.2 \times 10^{-4}$ and $\beta = 5/3$ for ρ in g cm^{-3} and T in eV. After some manipulation detailed elsewhere [7] and making the approximation that $R(T)$ represents the maximum radial spread about the centerline of the beam for secondary electrons with energy T , the dose (eV/unit volume) at a distance r from the ion track can be obtained:

$$D(r) = N_e \frac{Z_1^2 e^4}{8\pi\epsilon_0^2 m_e v_1 \beta r^2} \left(1 - \frac{r}{R_{max}} \right),$$

for $r \leq R_{max} = R(T_{max})$ (25.5)

The dependence of $D(r)$ on r , shown in Fig. 25.3(b) for 1 MeV protons in poly(methylmethacrylate) (PMMA), reveals that the electron dose is very sharply localized within a few nm from the ion track. Electron-mediated ion beam modification will thus be characterized by the superposition of intense localized electron doses extending along the ion tracks. Often one is interested in the net dose $D(p)$ at some point p in a material irradiated with a parallel flux of ions. This is the superposition of the dose $D(r_i)$ contributed by each of the ions impinging at a radial distance r_i from p within a radius R_{max} :

$$D(p) = \sum_{r_i \leq R_{max}} D(r_i) \quad (25.6)$$

R_{max} corresponds to the range of electrons with the maximum classical energy (25.5).

There exist a number of notable shortcomings in the simple track model outlined above.

- i. The model of the electron cascade ignores the lateral spreading of secondary electrons.
- ii. Only free classical excitation is considered, and resonant excitation is neglected.
- iii. The empirical assumption about electron ranges is in reasonable agreement with experiment in the keV region. However, because of the $1/T^2$ dependence of the differential scattering cross section in (25.2), most electrons will have lower energies, where the validity of the energy-range relation (25.4) is questionable and little experimental data exist.
- iv. The asymptotic behavior of $D(r)$ at small r – see (25.5) and Fig. 25.3 – is unphysical because the dose becomes infinite.
- v. Penetrating ions undergo lateral spreading as a result of nuclear and electronic scattering.

A complete treatment of the dose $D(r)$ about an ion track is analytically and computationally not straightforward [8] and requires a realistic 3-D calculation of electron slowing down, for example using Monte Carlo codes, such as CASINO [9–11], where the low-energy electronic stopping is determined from measurements of the complex optical refractive index and electron energy loss spectra [11]. In order to include the nuclear scattering contribution to the average dose $D(r)$ at a radius from the ion impingement axis, it is necessary to convolute $D(r)$ with the radial spreading from nuclear scattering events.

Plasma Column

The intense ionization along the ion track results from the rapid falloff with r of the radial dependence of the dose about an ion track (Fig. 25.3(b)). In the ion track, secondary electrons move radially away from the center, leaving behind less mobile positively charged holes. These exert an electrostatic restraining force on the electrons, which confines them to form a plasma column of electron-hole pairs some tens of nm broad that extends along the ion track. The plasma column may decay by spontaneous electron-hole recombination, releasing phonons (heat), or by ambipolar diffusion of electrons and holes out of the plasma column. The dominant mode of decay is determined by the electronic structure of the material. In metals, the electron-hole recombination dominates, whereas in semiconductors and dielectrics, the plasma column may be long-lasting and the column decays primarily by ambipolar diffusion rather than recombination. In dielectric materials, excitation may be so great that it introduces structural changes, for example by forming and breaking chemical bonds in polymers, and creating color center defects in alkali halides.

25.3 Applications of Materials Modification by MeV Ion Beams

25.3.1 MeV Implantation into Silicon Carbide (SiC)

The electrical, chemical, thermal and mechanical properties of silicon carbide (SiC) make electronic devices based on SiC superior to those based on Si for high-power and high-frequency applications, as well as for operation in harsh environments (e.g. high temperature and high radiation). Success in fabricating high-quality SiC has promoted worldwide activity in establishing technologies that make full use of this unique semiconductor.

For production of SiC-based devices, ion implantation is the only low-temperature doping technique because thermal diffusion of dopants requires extremely high temperatures. There is, however, a great challenge with ion implantation because it inevitably produces defects and lattice disorder, which not only deteriorate the transport properties of electrons and holes, but also inhibit electrical activation of the implanted dopants. Point defects or the growth of extended defect structures often leads to high leakage currents, poor and uneven injection during forward bias, and the premature breakdown under reverse bias observed in manufactured SiC diodes. To investigate the origin of these difficulties in SiC device fabrication and assess performance in high-radiation environments, MeV ions have been used to introduce damage into various SiC polytypes [12–19]. The disorder level of the atomic displacements or lattice disorder produced depends on the ion fluence, ion flux and implantation temperature. As an example, recent results [12, 19]

using 1.1 MeV Al_2^{2+} ions to investigate damage accumulation during ion bombardment are presented here.

The relative disorder on both the Si and the C sublattices at the damage peak for samples implanted at 150 K is shown in Fig. 25.4(a) [12]. The data indicate a predominantly sigmoidal dependence of the damage on increasing dose at the damage peak. At low ion fluence, the greater rate of C disordering is consistent with lower threshold displacement energy and a greater production rate of C defects relative to Si. These results are consistent with MD simulations of the displacement cascades [14]. MeV ion beams have also been used to study the annealing behavior. The example in Fig. 25.4(b) shows the recovery of relative Si disorder resulting from isochronal annealing [12]. Similar recovery behavior is observed for the C sublattice. In this process three distinct recovery stages are observed, which can be associated with mobile interstitials and vacancies in different defect configurations. Dynamic recovery of interstitials and vacancies is conspicuous during implantation at elevated temperatures [19]. This is illustrated in Fig. 25.5, which compares the disorder profiles for 1.1 MeV Al_2^{2+} implantations at 150 and 450 K. During

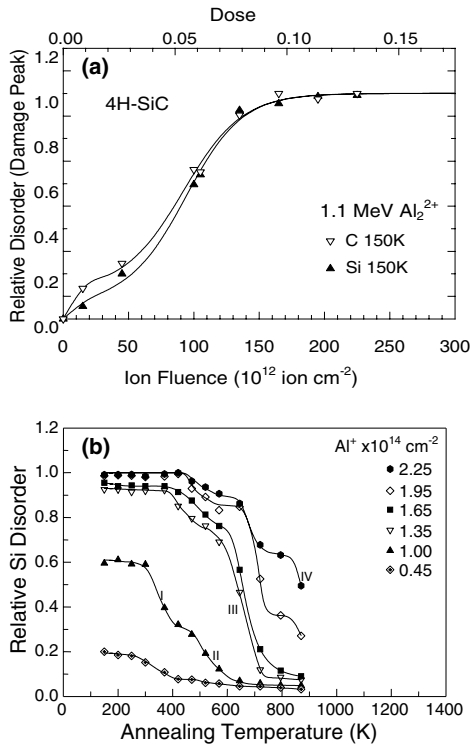


Fig. 25.4. (a) Relative disorder as a function of ion fluence for Al-implanted 4H-SiC. (b) Isochronal recovery of relative Si disorder at the damage peak

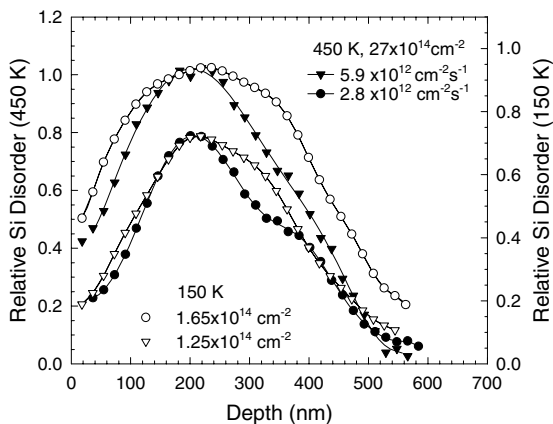


Fig. 25.5. The relative Si disorder profiles of samples that we implanted at different temperature, ion fluence and flux

implantation at 450 K, dynamic recovery of interstitials and vacancies occurs at a much higher rate, which suppresses the damage accumulation. The dynamic recovery implies that about 20 times higher fluence is needed at 450 K to produce the same damage level as at 150 K. The energy deposition rate through nuclear scattering can be controlled during MeV ion bombardment via the ion flux. Figure 25.6 shows high-resolution transmission electron microscope (HRTEM) images from the damage peak region. For the low-flux sample, as shown in Fig. 25.6(a), the basal-plane structure is maintained, while localized strain contrast is visible. Only a few occurrences of plane bending or termination are perceived. For the high-flux sample, a high concentration of planar defects and larger linked amorphous domains are observed, as shown in Fig. 25.6(b).

25.3.2 MeV Ion Irradiation Studies in Pyrochlore Materials

Pyrochlore materials ($A_2B_2O_7$) and perovskite-type oxides (ABO_3) are attracting great interest because of the capability to incorporate different elements in the A and B sites of their chemical structure. This capability suggests a wide range of applications, such as fuel cells [20, 21], catalysts [22, 23] and the immobilization of actinide-containing nuclear waste [24–29]. In actinide-bearing phases, considerable radiation damage due to alpha decay results in amorphization, macroscopic swelling and order-of-magnitude increases in dissolution rates [28–31]. This manifests itself as macroscopic changes in structure and chemical durability, which affect the long-term performance of the actinide waste forms [27–33].

Studies [29, 30, 34, 35] of actinide-doped/natural pyrochlores and related structures indicate that pyrochlores with Ti, Nb and Ta as the major B-site

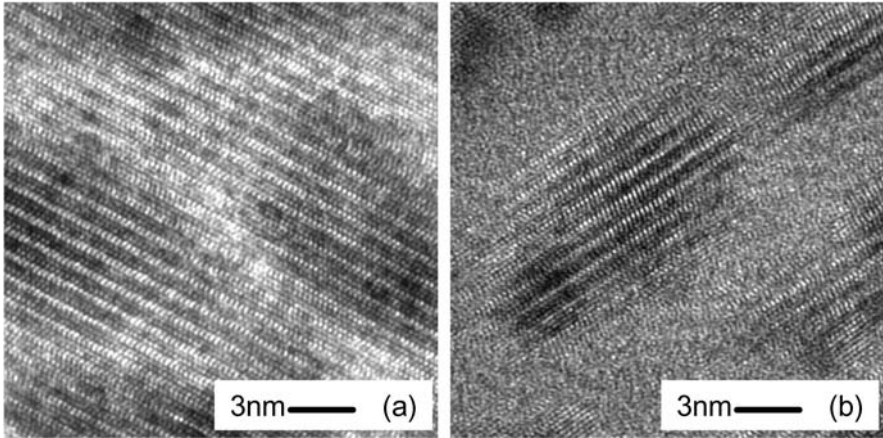


Fig. 25.6. HRTEM micrographs of samples implanted with 2.7×10^{15} 1.1 MeV Al_2^{2+} ions cm^{-2} at 450 K with different ion fluences (a) 2.8 and (b) 5.9×10^{12} Al^+ $\text{cm}^{-2} \text{s}^{-1}$

cations become amorphous as a result of the gradual accumulation of alpha-recoil collision cascades. These studies rely on the dose rates that can be achieved by radioactive decay and are hence time-consuming. Only limited data for a few sets of experimental conditions can generally be obtained.

More rapid evaluation of radiation effects in pyrochlore materials can be achieved by high-energy heavy-ion irradiation studies [25, 31, 36–39]. Alpha decay of actinide elements produces 4.5 to 5.8 MeV alpha particles and 70 to 100 keV recoil nuclei (alpha recoils). The more massive and lower-energy alpha recoils account for most of the damage produced through elastic-scattering collisions. Because the nuclear stopping of heavy ions is similar to the nuclear stopping of alpha recoils, the damage evolution under ion irradiation can provide a reasonable simulation of the damage evolution behavior due to alpha recoils. For actinide-containing pyrochlores, the radiation damage will be uniformly distributed. The nuclear damage induced in the surface layer by high-energy heavy ions is similar to that from the heavy alpha recoils because the cross sections and energy deposition are similar. MeV ion irradiation can be used to produce a highly damaged or amorphous state that does not differ greatly from that produced by alpha decay over long time periods. The power of this technique is that the highly damaged layers are confined to near-surface regions (up to several μm), and hence the chemical durability of such irradiated samples can be readily tested. The results of irradiation studies, as recently demonstrated for some pyrochlore samples [28], generally confirm the results for the highly damaged states of actinide-doped pyrochlores or natural minerals. Ion-beam irradiation provides a useful method to study amorphization, crystal swelling and dissolution rates and offers a reasonable

representation of the worst-case effect of radiation effects on chemical durability over long time periods for actual actinide-containing waste forms.

Implementation of the technique as a tool for testing pyrochlore materials for high-radiation environments requires quantitative studies of the damage evolution behavior as a function of irradiation dose and the mechanism for amorphization. Recently, the evolution of implantation-induced damage on the Sm and O sublattices from minor disorder to a fully amorphized state in samarium titanate pyrochlore ($\text{Sm}_2\text{Ti}_2\text{O}_7$) has been investigated [40]. In this study, 1 MeV Au^{2+} ions were chosen to simulate the damage production of heavy recoils through alpha decay. Rutherford backscattering spectroscopy (RBS) and $^{16}\text{O}(\text{d}, \text{p})^{17}\text{O}$ nuclear reaction analysis (NRA) along the $\langle 001 \rangle$ direction were used to characterize the relative disorder on the Sm and O sublattices, respectively. The damage accumulation at different irradiation temperatures is shown in Fig. 25.7. The results indicate that the relative

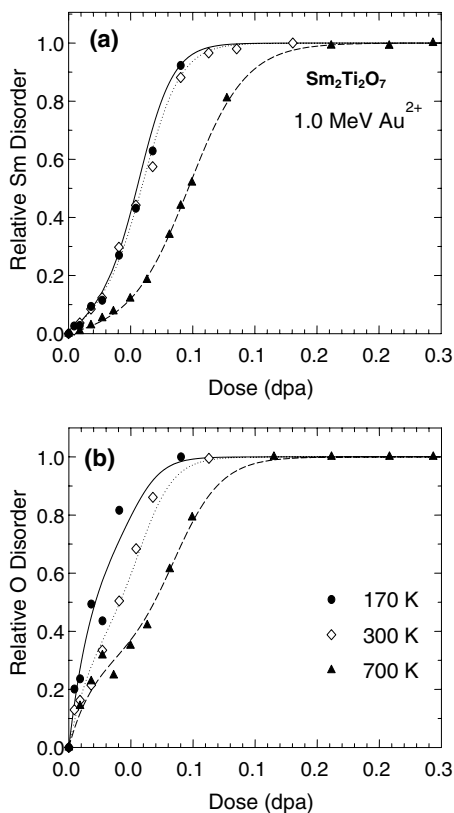


Fig. 25.7. Relative disorder at the damage peak on the (a) Sm and (b) O sublattices as a function of local dose for $\text{Sm}_2\text{Ti}_2\text{O}_7$ single crystals implanted with 1.0 MeV Au^{+} at 170, 300 and 700 K

disorder on each sublattice follows a nonlinear dose dependence and that the relative disorder on the O sublattice is higher than that on the Sm sublattice. There is little difference in damage accumulation on the Sm sublattice at 170 and 300 K. However, dynamic recovery processes dramatically reduce the rate of damage accumulation at 700 K.

The critical dose for amorphization in $\text{Sm}_2\text{Ti}_2\text{O}_7$ under irradiation by Au^{2+} [40] and Bi^+ [28] is shown in Fig. 25.8 as a function of irradiation temperature, together with the results for $\text{Gd}_2\text{Ti}_2\text{O}_7$ irradiated with Bi^+ [28]. Also included is the amorphization data point for alpha decay in $\text{Gd}_2\text{Ti}_2\text{O}_7$ doped with 3 wt% ^{244}Cm [41]. The critical temperature for amorphization, as shown in Fig. 25.8, is close to 975 K, which is similar to the onset temperature for the thermal recrystallization of Cm-doped $\text{Gd}_2\text{Ti}_2\text{O}_7$ [30]. Ion irradiation experiments accelerate the damage rates by six orders of magnitude, as compared with the 3 wt% ^{244}Cm -doped $\text{Gd}_2\text{Ti}_2\text{O}_7$. A good agreement of the amorphization dose at around room temperature (Fig. 25.8) is observed between the results of heavy-ion irradiation and the result obtained in ^{244}Cm -doped $\text{Gd}_2\text{Ti}_2\text{O}_7$ through alpha decay. This indicates that the dose-rate effect is negligible. These results provide some validation for applying models of damage accumulation and amorphization under heavy-ion irradiation to predict the long-term behavior in rare-earth titanates resulting from alpha decay.

One of the most exciting outcomes from fundamental studies of irradiation effects using ion beams has been the discovery of chemically durable and radiation-resistant $\text{Gd}_2\text{Zr}_2\text{O}_7$ and $\text{Er}_2\text{Zr}_2\text{O}_7$ pyrochlores. These materials can readily accommodate Pu on the Gd (or Er) and Zr sites [42]. In

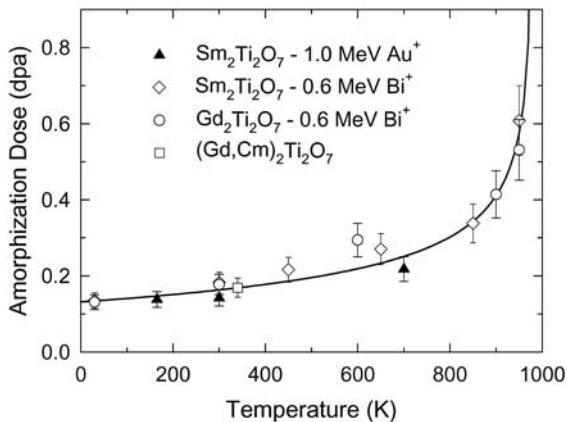


Fig. 25.8. Critical dose for amorphization of $\text{Sm}_2\text{Ti}_2\text{O}_7$ and $\text{Gd}_2\text{Ti}_2\text{O}_7$ irradiated by 1.0 MeV Au^{2+} and 0.6 MeV Bi^+ . Also included is the critical dose for amorphization in $\text{Gd}_2\text{Ti}_2\text{O}_7$ doped with 3 wt% ^{244}Cm . The solid curve is the best fit to the experimental data

general, the radiation resistance depends critically on the ability of the structure to sustain cation disorder on the A and B sites, as well as on a disordering of the oxygen vacancies. Irradiation studies have shown that the titanate–zirconate pyrochlore becomes more radiation-resistant with increasing zirconium concentration [25, 43]. Recent studies [24, 25, 39] demonstrate that pyrochlores of $\text{Gd}_2(\text{Ti}_{2-x}\text{Zr}_x)\text{O}_7$ display a dramatic decrease in susceptibility to radiation-induced amorphization with increasing Zr content. Pure zirconate end members undergo a radiation-induced transition to a disordered fluorite structure, which is highly radiation-resistant and remains crystalline to a high dose, for example 7.0 dpa (displacements per atom; see Appendix 25.A) for $\text{Gd}_2\text{Zr}_2\text{O}_7$ at 25 K [25] and 140 dpa for $\text{Er}_2\text{Zr}_2\text{O}_7$ at room temperature [24, 43]. In contrast, pure titanate end member pyrochlores are sensitive to irradiation damage and readily become amorphous (0.4 dpa [28] for $\text{Gd}_2\text{Ti}_2\text{O}_7$ at 900 K, 0.18 dpa [28] for $\text{Gd}_2\text{Ti}_2\text{O}_7$ and 0.26 dpa [24, 43] for $\text{Er}_2\text{Ti}_2\text{O}_7$ at 300 K).

25.3.3 Radiation Damage and Mixing

Ion beam mixing and the damage induced with MeV ions and keV ions are closely similar. Nuclear scattering leads to atomic displacements so that different layers of materials become ballistically mixed. In addition, non-thermalized defects can also promote diffusion. This provides a convenient method to atomically mix materials even when they form a multiphase structure under thermodynamic equilibrium conditions. An example of the use of MeV ion beam mixing is modification of the band gap in quantum well structures by mixing the quantum well with the adjacent layers, followed by epitaxial regrowth to recover the radiation damage. Figure 25.9 illustrates the mixing of $\text{InP}/\text{Ga}_{0.25}\text{In}_{0.75}\text{As}/\text{InP}$ quantum wells using channeled 10 MeV $^{69}\text{Ga}^+$ ions [44]. This resulted in a blue shift (band gap increase) of about 30 meV (Fig. 25.9(b)). A novel feature was the lateral writing of the degree of blue shift by using a thin Au dechanneling mask to modulate the degree of channeling and hence the degree of ion beam mixing [44] (Fig. 25.9(b)). An alternative route to lateral definition is to use focused ion beams. Low-energy focused 0.16 MeV Si^{2+} ions have been used for direct writing of waveguides in a $\text{GaAlAs}/\text{GaAs}$ superlattice material for distributed-feedback (DFB) lasers [45], whilst 1 MeV Co has been used to synthesize CoSi_2 structures [46].

25.3.4 Electron-Induced Interactions

The strong coupling of the kinetic-energy loss of a penetrating ion with the electronic system of the material may be used to modify materials where electronic excitations can lead to latent or direct material changes. Generally, in metals, the electronic relaxation time is so short that the electronic excitation rapidly dissipates as phonons before atomic displacement takes place.

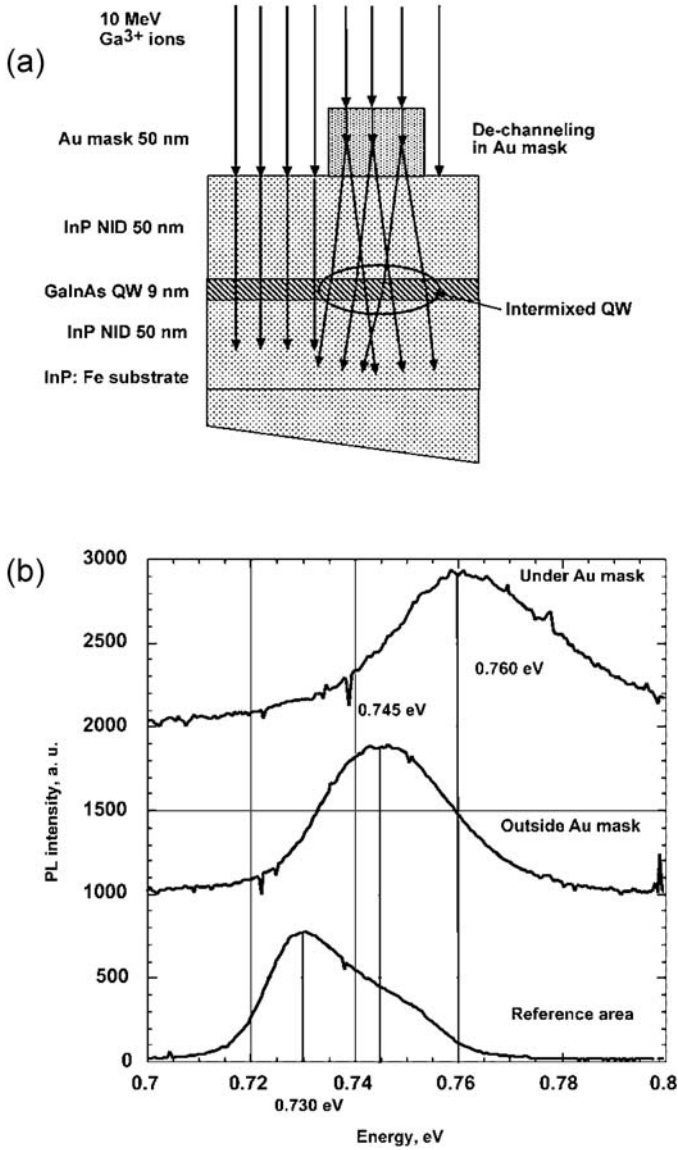


Fig. 25.9. (a) Schematic illustration of switched-channeling MeV ion beam mixing of an InP/Ga_{0.25}In_{0.75}As/InP quantum well structure. (b) Photoluminescence measurement of the band gap change [44]

In materials with a band gap, the excitation from the ion and the secondary electrons and recoils can introduce a number of changes, such as excitation across the band gap as well as to and from defect levels. If the energy available exceeds the amount required to cleave bonds, these may be broken at random. These broken bonds can relax by forming new bond configurations, which in turn change material properties such as refractive index, optical absorption, conductivity, chemical resistance and density. MeV ions have been employed to introduce changes in the refractive index in glasses [47, 48] and introduce photoluminescence centers in silica [49].

An important class of materials where electron-mediated interactions are significant is polymers. These form the basis of the organic resists used in lithography, discussed below. The polymer can be either a positive resist (such as PMMA), where ion irradiation causes chain scission [50] that locally reduces the molecular weight of the polymer chains, or a negative resist (such as epoxies) where crosslinking [50] is induced. After exposure, the latent image is developed in a selective solvent that preferentially dissolves low-molecular-mass chains (positive resists) or noncrosslinked chains (negative resists).

25.3.5 Nanoscale Lithography with MeV ion Beams

Nanoscience and nanotechnology is one of the most exciting and important areas of research today. This is a truly cross-disciplinary research field with a major impact on forefront research in fields as diverse as cell biology and medicine and quantum electronics and optics. One of the big challenges in nanoscale engineering is the development of technologies that can be scaled up from the single devices produced in the research laboratory, first to fabricate large numbers of them in defined configurations to realize circuits, and subsequently to manufacture these circuits in industrial quantities. The active parts of quantum devices based on quantum confinement and tunneling are typically less than 5 nm in size. High-packing-density circuits using these components will require lithographic processing of interconnects on a similar size scale. In semiconductor technology, the well-known Moore's law predicts a halving of feature sizes and doubling of the number of devices per circuit every 18 months. At the time of writing, very large-scale integration (VLSI) devices are routinely produced with a 0.13 μm line width, and 0.09 μm is at the pilot stage. The EU Nanoelectronics Roadmap [51] points to industrial maturity for 70 nm line width features by 2008. Similar trends are seen in magnetic information storage, where the size of the domains (bits) is shrinking to similar sizes, and this implies that new approaches are needed to keep the domains separated. In order to realize this, there is a clear need for new lithographic tools that can extend the writing capability to better resolution than that achievable with the current industry-piloted extreme ultraviolet (EUV) projection lithography (30–50 nm [51]).

Focused MeV ions, such as used in the nuclear microprobe discussed in Chap. 26, can also be used for the lithographic writing of latent or permanent patterns of modified material. Over the past 5 years or so, the proton-beam-writing (PBW) technique that has been pioneered by the Singapore group [53, 54] has attracted interest, not least because of its 3-dimensional writing capability [55]. In PBW, the protons are focused to a $30\text{ nm}-2\text{ }\mu\text{m}$ spot size that is used to write a latent pattern by modifying a resist polymer (discussed above) coated on a substrate material. The writing is done by modulating the intensity of the beam as the spot is scanned over the sample. After developing, the resist is fully developed at points where the dose (25.6) exceeds the *clearing dose*. The clearing dose is the dose needed to just produce a fully developed latent pattern so that, after development, the polymer is either completely removed (positive resist) or completely retained (negative resist).

The smallest feature size that can be written is determined by the extent of the region where the dose exceeds the clearing dose. The minimum size of a feature is then governed by the spreading of the dose about the axis of the beam. This is, in essence, the convolution of an extrinsic contribution from the beam focus profile and an intrinsic contribution associated with the spreading of the ion beam, secondary recoils and electrons in the target. Reference to Fig. 25.2 shows that in the outer few hundred nanometers the radial spreading of the ion beam is a nanometer or so. This, combined with the sharp falloff of the dose from secondary electrons $D(r)$ within a 10 nm radius of the track (Fig. 25.3(b)), allows extremely high-aspect structures with 60 nm wide walls in $10\text{ }\mu\text{m}$ thick resist to be written [56]. An example is shown in Fig. 25.10, which shows a pattern written in negative SU-8 resist for use as an etch mask for plasma etching of thin silicide lines. In this case a negative resist was chosen to selectively protect the surface during subsequent plasma etching. Another important factor is the proximity exposure effect. If

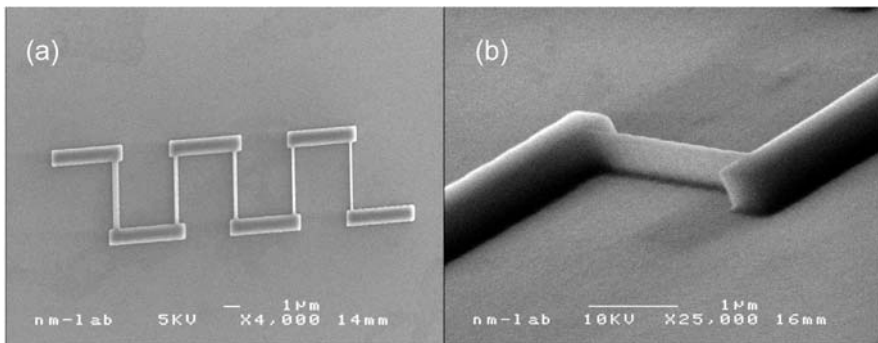


Fig. 25.10. Plasma etch mask produced in SU-8 resist [52] by PBW. The smallest vertical line in (a) is 120 nm wide. (b) Tilted view of the 120 nm line (H.J. Whitlow, I. Maximov, L. Montelius, J. van Kan, A. Bettiol and F. Watt, unpublished data)

the pattern has large, closely spaced exposed areas, the unirradiated region in between receives a dose because of spreading of the dose distribution beyond the edges of the irradiated regions. For PBW, this is much smaller than is the case for the 10–40 keV electrons used in conventional focused-electron-beam lithography (EBL) [57]. This is because, as discussed in Sect. 25.2.4, in PBW the majority of δ -electrons are directed perpendicular to the beam with energies close to zero and hence have short ranges. This gives an extremely sharp radial dose distribution $D(r)$ as shown in Fig. 25.3(b). The small proximity effect for PBW facilitates writing high-spatial-density patterns that would be extremely difficult to write using conventional EBL because of the proximity effect. An example of a high-spatial-density structure that has been written with PBL is shown in Fig. 25.11. This shows a metal pattern produced by metal lift-off using a 170 nm thick positive PMMA resist. Here a positive resist was used, and consequently the area where metal was to be deposited was irradiated. The pattern is a prototype interdigitated electrode array for electrochemical biosensors capable of assaying specific biomolecules such as antigens, antibodies and hormones [57]. The use of PBW enabled wide electrodes with narrow gaps to be written, which is particularly difficult using conventional EBL. Small (~ 100 nm) gaps can also be written using PBW in negative resist, as shown in Fig. 25.12, which shows an Au-coated finger structure in negative SU-8 resist, where the 100 nm gap between the fingers is clearly seen.

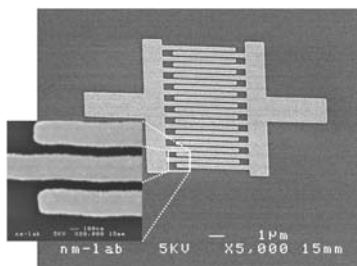


Fig. 25.11. Interdigitated metal pattern with nanoscale electrode gaps for biosensor development, fabricated using PBW. The metal pattern is 30 nm Au/3 nm Ti on a SiO_2/Si substrate. PBW was used to produce an aperture pattern in a 170 nm thick positive PMMA resist prior to metal evaporation, followed by lift-off of metal by dissolution of the resist from unexposed regions in hot acetone [57]

PBW is not restricted to writing latent images. Patterns of direct changes in the refractive index and photoluminescence of glassy materials can be written [47–49]. The changes in molecular structure in polymers subject to MeV ion bombardment also cause direct changes in the density and refractive index [58]. These changes are most pronounced in the end-of-range damage. A spectacular application of this phenomenon is the direct writing of buried

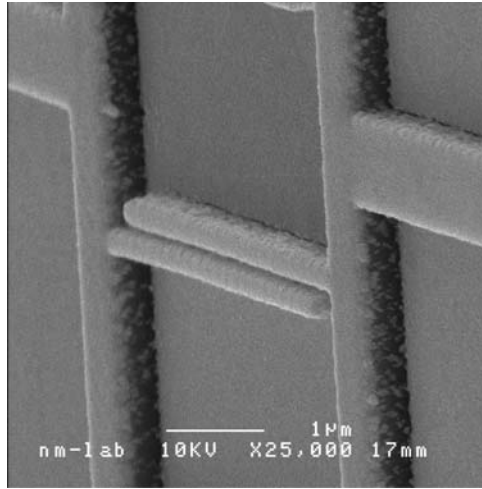


Fig. 25.12. Detail of PBW finger structure in negative resist coated with 100 nm Au (H.J. Whitlow, I. Maximov, L. Montelius, J. van Kan, A. Bettiol and F. Watt, unpublished data)

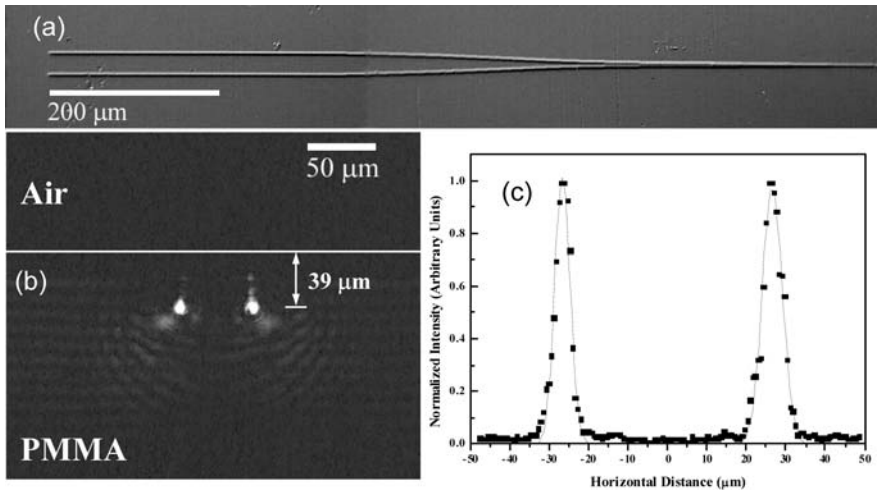


Fig. 25.13. Buried y-branch optical-waveguide structure produced in PMMA by direct writing with 1.5 MeV protons. (a) Differential interference contrast image of the waveguide structure. (b) 633 nm laser light emitted from the branches. (c) Normalized intensity of the light distribution in (b) (Reprinted from [59], copyright 2003, with permission from Elsevier)

optical-waveguide structures [59]. Figure 25.13 shows an optical-waveguide structure fabricated by direct writing with 1.5 MeV $^1\text{H}^+$ in PMMA by the Singapore group [59], the emitted 633 nm light observed with a CCD camera from the branches of a 2 mm y-branch waveguide, and the corresponding intensity distributions.

Acknowledgments

We are grateful to our collaborators at Pacific Northwest National Laboratory, The Nanometer Consortium in Lund and The Centre for Ion Beam Applications at the National University of Singapore for assistance, guidance and permission to use figures. One of the authors (YZ) acknowledges the support of the Division of Materials Sciences and Engineering Office of Basic Science, U.S. Department of Energy.

25.A Appendix: Nomenclature in SI Units

Displacements per atom (dpa). The mean number of times an atom is displaced from its atomic site. This quantity is a measure of the dose in terms of the mean number of displacements from its site that an atom undergoes.

Dose. SI-defined unit, which is the energy absorbed per unit mass of material [60,61]. The unit is the gray (Gy) = 1 J kg^{-1} , or, in terms of SI base units [62], $\text{m}^2 \text{ s}^{-2}$. A related quantity in radiation physics with the same units is the kerma K (kinetic energy released per unit mass) [63] which is the sum of all of the kinetic energy of all charged particles created by uncharged ionizing particles. It is a measure of the dose deposited by uncharged particles, such as X-ray photons.

Electron volt (eV). Energy is often expressed in electron volts; an electron volt is the energy gained by an electron on passing through a potential difference of 1 volt. The eV is not an SI unit but it is accepted for use with the SI [62].

G value. The number of specified chemical events in an irradiated substance produced per 100 eV of energy absorbed from ionizing radiation.

Linear energy transfer (LET). The average energy locally imparted to a medium by a charged particle of specified energy, per unit distance traversed. The LET is not a unit of fundamental significance.

Mass stopping power ε^* . This quantity is the stopping power, where the distance is expressed in terms of mass per unit area: $\varepsilon^* = (1/\rho) dE/dx$.

Particle flux \dot{N} . This is the ratio of the infinitesimal change in the particle number dN to an infinitesimal time interval dt . $\dot{N} = dN/dt$. The units are s^{-1} .

Particle fluence Φ . This is defined [61] as the number of particles dN crossing the surface of a sphere with cross-sectional area dA . $\Phi = dN/dA$. The units are m^{-2} ; however, for convenience quantity is often given in terms of cm^{-2} . For ion beam applications where parallel ions are incident on a planar reference surface, care should be exercised because the particle fluence does not explicitly define the direction. In this case it may be advisable to specify the beam direction, for example “the fluence of ions normally incident on the surface was $3 \times 10^{18} \text{ m}^{-2}$ ”. It is recommended that the term “particle fluence” or “ion fluence” is used to avoid confusion with the use of “fluence” in radiation chemistry to specify the dose rate [64].

Particle fluence rate ϕ . This is the time differential of the particle fluence; $\phi = d^2N/(dt dA)$. The units are $\text{m}^{-2} \text{ s}^{-1}$. Often the term “particle flux density” has been used; however, “particle flux rate” is preferred [61].

Particle fluence differential in energy Φ . This is the fluence of particles in the energy interval E to $E + dE$. $\Phi(E) = d\Phi/dE$ [61].

Stopping cross section ε . The stopping cross section is the energy loss per atom per unit area. $\varepsilon = dE/(N_a dx)$, where N_a is the number of atoms per unit volume. It is usually given in units of $\text{eV}/10^{15} \text{ at cm}^{-2}$. As a rule of thumb, the value in these units is of the order of the energy loss per monolayer in a typical solid material [64].

Stopping force (stopping power) dE/dx . This quantity is the mean energy loss per unit path length, with units J m^{-1} , and has the dimensions of a force and should correctly be termed “stopping force” [65]. For practical applications, the stopping force is often given in units of eV/nm or $\text{eV}/\mu\text{m}$. The term “stopping power” has been widely used in the literature.

References

1. N. Nastasi, J.W. Mayer, J.K. Hirvonen: *Ion-Solid Interactions: Fundamentals and Applications* (Cambridge University Press, London 1996)
2. J.F. Ziegler, J.P. Biersack, U. Littmark: *The Stopping and Ranges of Ions in Matter*, vol. 1 (Pergamon, New York 1985); SRIM 2003.24, <http://www.srim.org>.
3. M.W. Thompson: *Defects and Radiation Damage in Metals* (Cambridge University Press, London 1969).
4. H.H. Andersen: *Forelæsning over Strålningsbeskadelse i faste stoffer 1. Defektproduktion og defektkonfigurationer* (Det fysiske institut, Aarhus universitet, Aarhus 1984)
5. P. Sigmund: Nucl. Instr. Meth. B **135**, 1 (1998)
6. N. Bohr: Det. Kgl. Danske Videnskabernes Selskab, Matematisk-fysiske Meddelelser **18**, Nr. 8 (1948)
7. R. Spohr: In *Ion Tracks in Microtechnology, Principles and Applications*, ed. by K. Bethge (Vieweg, Braunschweig 1990) p. 112

8. P. Sigmund: Nucl. Instr. Meth. B **164–165**, 401 (2000)
9. P. Hovington, D. Drouin, R. Gauvin: Scanning **19**, 1 (1997)
10. D. Drouin, P. Hovington, R. Gauvin: Scanning **19**, 20 (1997)
11. P. Hovington, D. Drouin, R. Gauvin, D.D. Joy, N. Evans: Scanning **19**, 29 (1997)
12. Y. Zhang, W.J. Weber, W. Jiang, A. Hallén, G. Possnert: J. Appl. Phys. **91**, 6388 (2002)
13. W. Jiang, W.J. Weber: Phys. Rev. B **64**, 125206 (2001)
14. F. Gao, W.J. Weber: Phys. Rev. B **63**, 054101 (2001)
15. L. Henry, M.F. Barthe, C. Corbel, P. Desgardin, G. Blondiaux, S. Arpiainen, L. Liskay: Phys. Rev. B **67**, 115210 (2003)
16. X.D. Chen, C.C. Ling, S. Fung, C.D. Beling, M. Gong, T. Henkel, H. Tanoue, N. Kobayashi: J. Appl. Phys. **93**, 3117 (2003)
17. W.J. Weber, N. Yu, L. M. Wang: J. Nucl. Mater. **253**, 53 (1998)
18. R.E. Avila, J.J. Kopanski, C.D. Fung: J. Appl. Phys. **62**, 3469 (1987)
19. Y. Zhang, W.J. Weber, W. Jiang, C.M. Wang, A. Hallén, G. Possnert: J. Appl. Phys. **93**, 1954 (2002)
20. H.L. Tuller: J. Phys. Chem. Solids **55**, 1393 (1994)
21. B.J. Wuensch, K.W. Eberman, C. Heremans, E.M. Ku, P. Onnerud, E.M.E. Yeo, S.M. Haile, J.K. Stalick, J.D. Jorgensen: Solid State Ionics **129**, 111 (2000)
22. J.B. Goodenough, R.N. Castellano: Solid State Chem. **44**, 109 (1982)
23. S.J. Korf, H.J.A. Koopmans, B.C. Lippens, A.J. Burggraaf, P.J. Gellings: J. Chem. Soc. Faraday Trans. **83**, 1485 (1987)
24. K.E. Sickafus, L. Minervini, R.W. Grimes, J.A. Valdez, M. Ishimaru, F. Li, K.J. McClellan, T. Hartmann: Science **289**, 748 (2000)
25. S.X. Wang, B.D. Begg, L.M. Wang, R.C. Ewing, W.J. Weber, K.V. Godivan Kutty: J. Mater. Res. **14**, 4470 (1990)
26. R. C. Ewing, W. J. Weber, and J. Lian, J. Appl. Phys. **95**, 5949 (2004)
27. R.C. Ewing, W.J. Weber, W. Lutze: In *Diposal of Weapon Plutonium*, ed. by E.R. Merz, C.E. Walter (Kluwer Academic Dordrecht 1996) p. 65
28. B.D. Begg, N.J. Hess, W.J. Weber, R. Devanathan, J.P. Icenhower, S. Thevuthasan, B.P. McGrail: J. Nucl. Mater. **288**, 208 (2001)
29. W.J. Weber, J.W. Wald, Hj, Matzke: Mater. Lett. **3**, 173 (1985)
30. W.J. Weber, J.W. Wald, Hj, Matzke: J. Nucl. Mater. **138**, 196 (1986)
31. B.D. Begg, W.J. Weber, R. Devanathan, J.P. Icenhower, S. Thevuthasan, B.P. McGrail: Ceram. Trans. **107**, 553 (2000)
32. R.C. Ewing, W.J. Weber, F.W. Clinard Jr.: Prog. Nucl. Energy **29**, 63 (1995)
33. W.J. Weber, R.C. Ewing, C.R.A. Catlow, T. Diaz de la Rubia, L.W. Hobbs, C. Kinoshita, Hj. Matzke, A.T. Motta, M. Nastasi, E.K.H. Salje, E.R. Vance, S.J. Zinkle: J. Mater. Res. **13**, 1434 (1998)
34. F.W. Clinard Jr., D.E. Peterson, D.L. Rohr, L.W. Hobbs: J. Nucl. Mater. **126**, 245 (1984)
35. G.R. Lumpkin: J. Nucl. Mater. **289**, 136 (2001)
36. R.C. Ewing, L.M. Wang: Nucl. Instr. Meth. Phys. Res. B **65**, 319 (1992)
37. S.X. Wang, L.M. Wang, R.C. Ewing, G.S. Was, G.R. Lumpkin: Nucl. Instr. Meth. Phys. Res. B **148**, 704 (1999)
38. W.J. Weber, N.J. Hess: Nucl. Instr. Meth. Phys. Res. B **80–81**, 1245 (1993)
39. B.D. Begg, N.J. Hess, D.E. McCready, S. Thevuthasan, W.J. Weber: J. Nucl. Mater. **289**, 188 (2001)

40. Y. Zhang, W.J. Weber, V. Shutthanandan, R. Devanathan, S. Thevuthasan, G. Balakrishnan, D.M. Paul: *J. Appl. Phys.* **95**, 2866 (2004)
41. W.J. Weber, R.C. Ewing: In *Scientific Basis for Nuclear Waste Management XXV*, ed. by B.P. McGrail, G.A. Cragolino, Mater. Res. Soc. Symp. Proc. 713, (Materials Research Society, Warrendale, PA 2002) p. 443
42. R.E. Williford, W.J. Weber: *J. Nucl. Mater.* **299**, 140 (2001)
43. K.E. Sickafus, L. Minervini, R.W. Grimes, J.A. Valdez, T. Hartmann: *Radiat. Eff. Defects Solids* **155**, 133 (2001)
44. T. Winzell, I. Maximov, L. Landin, Y. Zhang, A. Gustafsson, L. Samulelsson, H.J. Whitlow: *Semicond. Sci. Technol.* **16**, 889 (2001)
45. A. Steckl, P. Chen, H.E. Jackson, A.G. Choo, X. Cao, J.T. Boyd, M. Kumar: *J. Vac. Sci. Technol. B* **13**, 2570 (1995)
46. J. Meyer, U. Weidenmüller, P. Baving, H. Röchen, A. Stephan, H.H. Bukow, C. Rolfs: *Nucl. Instr. Meth. B* **161–163**, 898 (2000)
47. M. Hattori, Y. Ohki, M. Fujimaki, T. Souno, H. Nishikawa, E. Watanabe, M. Oikawa, T. Kamiya, K. Arakawa: *Nucl. Instr. Meth. B* **210**, 272 (2003)
48. I. Rajta, I. Gómez-Morilla, M.H. Abraham, Á.Z. Kiss: *Nucl. Instr. Meth. B* **210**, 260 (2003)
49. T. Souno, H. Nishikawa, M. Hattori, Y. Ohki, E. Watanabe, M. Oikawa, T. Kamiya, K. Arakawa: *Nucl. Instr. Meth. B* **210**, 277 (2003)
50. A. Chapiro: *Nucl. Instr. Meth. B* **32**, 111 (1988)
51. R. Compañó: *Technology Roadmap for Nanoelectronics*, 2nd ed., European Commission IST program Future and Emerging Technologies (2000)
52. Micro Chem, 1254 Chestnut Street, Newton, MA 02464, USA: http://www.microchem.com/products/su_eight.htm
53. J.A. van Kan, T.C. Sum, T. Osipowiz, F. Watt: *Nucl. Instr. Meth. B* **161–163**, 366 (2000)
54. T. Osipowicz, J.A. van Kan, T.C. Sum, J.L. Sanchez, F. Watt: *Nucl. Instr. Meth. B* **161–163**, 83 (2000)
55. J.A. van Kan, J.L. Sanchez, T. Osipowicz, F. Watt: *Microsyst. Technol.* **6**, 82 (2000)
56. J.A. van Kan, A.A. Betiol, F. Watt: *Appl. Phys. Lett.* **83**, 1629 (2003)
57. H.J. Whitlow, M.L. Ng, V. Auželyté, I. Maximov, L. Montelius, J.A. van Kan, A. Bettiol, F. Watt: *Nanotechnology* **15**, 223 (2003).
58. A.A. Betiol, T.C. Sum, J.A. van Kan, F. Watt: *Nucl. Instr. Meth. B* **210**, 250 (2003)
59. T.C. Sum, A.A. Betiol, H.L. Seng, I. Rajta, J.A. van Kan, F. Watt: *Nucl. Instr. Meth. B* **210**, 266 (2003)
60. ICRU Report 33, *Radiation Quantities and Units* (International Commission on Radiation Units and Measurements, 1980)
61. <http://www.npl.co.uk/ionrad/quantities.html>
62. Bureau International des Poids et Mesures, Pavillon de Breteuil, 92312 Sèvres Cedex, France: <http://www.bipm.fr/enus/>
63. <http://rkb.home.cern.ch/rkb/PH14pp/node154.html#153>
64. A.D. McNaught, A. Wilkinson; *Compendium of Chemical Terminology: The Gold Book*, 2nd edn. (International Union of Pure and Applied Chemistry), Internet edition, <http://www.iupac.org/publications/compendium/index.html>
65. P. Sigmund: ICRU News, June 2000, p. 5